Cavitation Erosion

Marc C. Fivel, Jean-Pierre Franc

Cavitation Erosion

Marc FIVEL
Science and Engineering of Materials and Processes (SIMAP)
http://simap.grenoble-inp.fr/
Marc.Fivel@simap.grenoble-inp.fr

Jean-Pierre FRANC
Laboratory of Geophysical and Industrial Flows (LEGI)
http://legi.grenoble-inp.fr/
Jean-Pierre.Franc@legi.cnrs.fr

CNRS – Grenoble Institute of Technology – Université Grenoble Alpes

1 Introduction to cavitation

The term cavitation is commonly used by the fluid mechanics community to describe the growth of bubbles within a liquid due to low pressures. Figure 1 shows a typical example of cavitation bubbles that develop on the upper side of a hydrofoil in a cavitation tunnel.

Figure 1: Typical example of cavitation on a hydrofoil. The hydrofoil is mounted in the hydrodynamic tunnel of LEGI at a positive angle of attack. Flow of water is from left to right. Chord length is 10 cm. Cavitation bubbles originate from microbubbles or cavitation nuclei carried by the liquid flow. They are activated by the low pressure region that exists near the leading edge of the hydrofoil. They grow to macroscopic cavitation bubbles before collapsing more downstream in the region where the pressure is recovered.

Although cavitation might appear similar to boiling, there is a big difference between the two. This is illustrated in Figure 2 where the phase diagram of water has been plotted from classical equilibrium thermodynamics. The liquid and vapor domains are easily identified depending upon pressure and

temperature. They are separated by the vapor pressure curve that extends from the triple point to the critical point. For boiling, phase change occurs along a horizontal path in this diagram (i.e. at constant pressure) and for increasing temperatures caused by heat supply. On the other hand, cavitation occurs along a vertical path (i.e. at almost constant temperature) and for decreasing pressures.

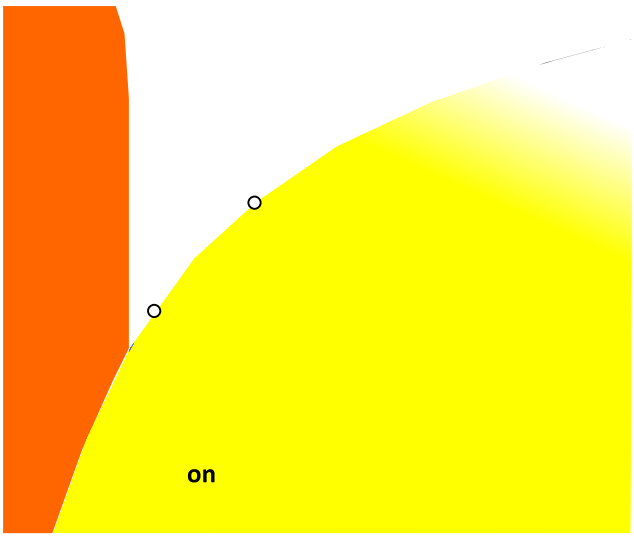

Figure 2: Phase diagram of water. The solid line that connects the triple point and the critical point is the vapor pressure curve. It separates the liquid domain from the vapor domain.

From Figure 2, it is clear that the critical pressure for cavitation inception is the conventional equilibrium vapor pressure where liquid is expected to turn into its vapor. Even though there might be deviations from this simple rule, the vapor pressure is generally considered as the critical parameter for the inception of cavitation. At the ambient temperature of 20°C, vapor pressure for water is about 2300 Pa or 0.023 atm. If pressure in liquid water drops locally below this critical value, cavitation is expected. The question is to know how the pressure may drop in a liquid flow.

Consider the case of hydrodynamic cavitation, as in many industrial applications such as pumps, hydraulic turbines or valves. Hydrodynamic cavitation that occurs in a flowing liquid is generally opposed to vibratory cavitation that occurs in a nearly static liquid. A typical example of vibratory cavitation is given in Section 3 with ultrasonic devices. In the case of hydrodynamic cavitation, the

pressure drop that may trigger cavitation can easily be understood from the well-known Bernoulli equation:

$$p + \frac{1}{2}\rho V^2 = Constant \tag{0.1}$$

In this equation, p and V are the local pressure and velocity of the liquid and ρ its density. This equation expresses the balance of energy between the kinetic energy of the liquid and its potential energy in terms of pressure. As a result, any local increase in the liquid velocity generates a local decrease in pressure. If the pressure drops below the vapor pressure at the operating temperature, cavitation appears. In practice, a local increase in velocity is expected for instance in contractions or around blades (see Figure 1), with consequently a decrease in pressure and a risk of cavitation.

Cavitation in a liquid flow can take different forms. In addition to the case of traveling bubble cavitation shown in Figure 1, let us mention:

- attached cavitation which is characterized by a vapor cavity often attached to the leading edge of a blade or hydrofoil (Figure 3)

- vortex cavitation where cavitation develops in the core of vortices such as the vortex produced at the tip of a propeller blade or three-dimensional hydrofoil (Figure 4)

- shear cavitation that develops either in turbulent wakes of bluff bodies (Figure 5) or in high speed submerged jets.

Although cavitation may have beneficial effects e.g. in medicine [1-3], surface cleaning [4] or water treatment [5, 6], it is often recognized for its harmful consequences in industry such as performance breakdown, noise, vibration and more especially erosion [7], which is the subject of the present paper.

This paper is devoted to the damage induced by the only mechanical action of the collapsing bubbles without any additional electrochemical effect as it may be the case in corrosive environments such as in seawater systems [8-11]. For corrosive liquids, a synergetic effect of cavitation and corrosion has been reported in the literature so that the overall damage rate is larger than the sum of the pure corrosion damage rate and the pure cavitation erosion rate. This is generally explained by the fact that cavitation mechanically removes the passivating corrosion film and, as a result, opens fresh highly reactive corrosion sites.

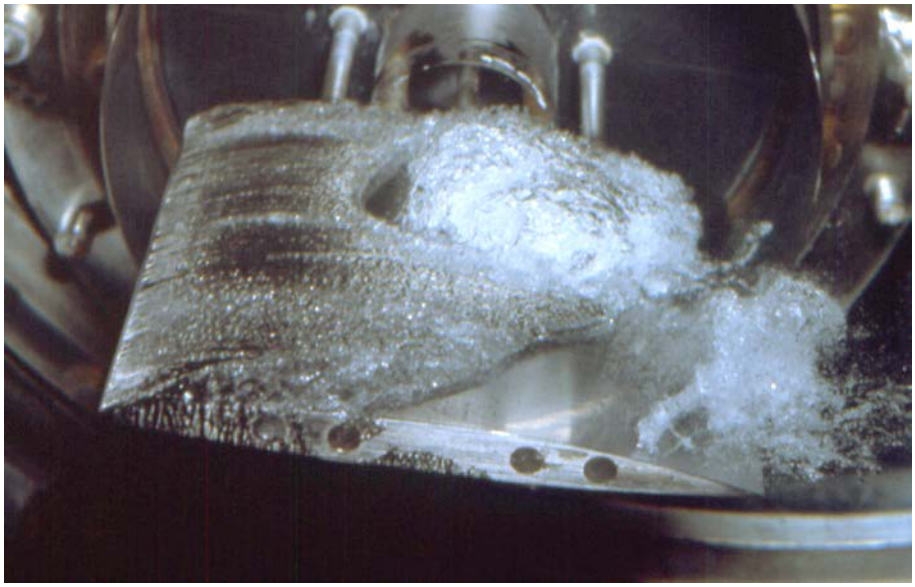

Figure 3: Typical example of attached cavitation. The cavity detaches from the leading edge of the hydrofoil. The cavity closure region is very unsteady and sheds, more or less periodically, clouds of vapor bubbles that are known to be particularly aggressive from an erosion viewpoint (LEGI hydrodynamic tunnel).

Figure 4: Typical example of tip vortex cavitation. The tip vortex is generated by a three-dimensional hydrofoil. Cavitation fills the core of the tip vortex where the pressure drops because of centrifugal forces (LEGI hydrodynamic tunnel).

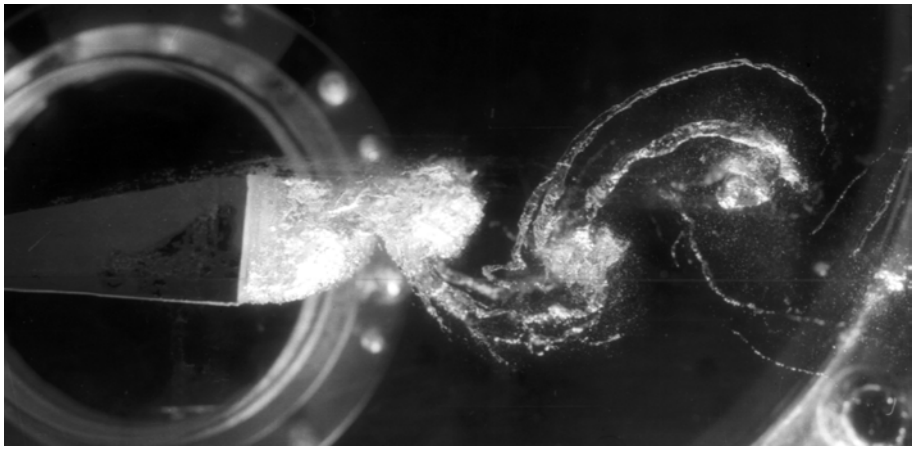

Figure 5: Typical example of shear cavitation. Cavitation is generated here in the turbulent wake of a bluff body. Various types of cavitating vortices are produced including two-dimensional Benard-Karman vortices and three-dimensional streamwise vortices (LEGI hydrodynamic tunnel).

2 Mechanism of cavitation erosion

A typical example of cavitation erosion damage is shown in Figure 6. Generally speaking, damage is due to the collapse of cavitation bubbles that generate each a high impulsive load when collapsing. As explained in Section 1, cavitation bubbles grow in low-pressure regions of the liquid flow. They are transported by the flow and collapse when entering regions of pressure recovery. Collapse is usually violent because the pressure inside a cavitation bubble (which remains equal to the vapor pressure all along the collapse, typically 0.023 atm for water at room temperature) is very small in comparison to the ambient pressure typically of the order of the atmospheric pressure. Thus, the bubble content offers almost no resistance to the collapse and the velocity of the bubble wall increases continuously. The surrounding liquid also gains a high velocity and, when it hits the wall, an impulsive load of high intensity is generated that may cause a microscopic damage. Because of the large number of cavitation bubbles and their random distribution in the flow field partly due to turbulence, the superposition of such single collapses leads to a macroscopic damage that progressively increases with time of exposure to cavitation.

The dynamics of a spherical cavitation bubble can be described by the Rayleigh-Plesset equation. A simplified form of this equation that neglects the effects of surface tension, viscosity and non-condensable gas is the Rayleigh equation [12, 13]:

$$R\ddot{R} + \tfrac{3}{2}\dot{R}^2 = -\frac{p_\infty - p_v}{\rho} \tag{0.2}$$

where R is the bubble radius, p_v the vapor pressure, p_∞ the pressure applied to the bubble that makes it collapse and ρ the liquid density. The quantities $\dot{R}$ and $\ddot{R}$ denote the first and second derivatives of the bubble radius with respect to time. The dynamics of a spherical cavitation bubble when subjected to a given pressure p_∞ can be approached by solving this second-order differential equation.

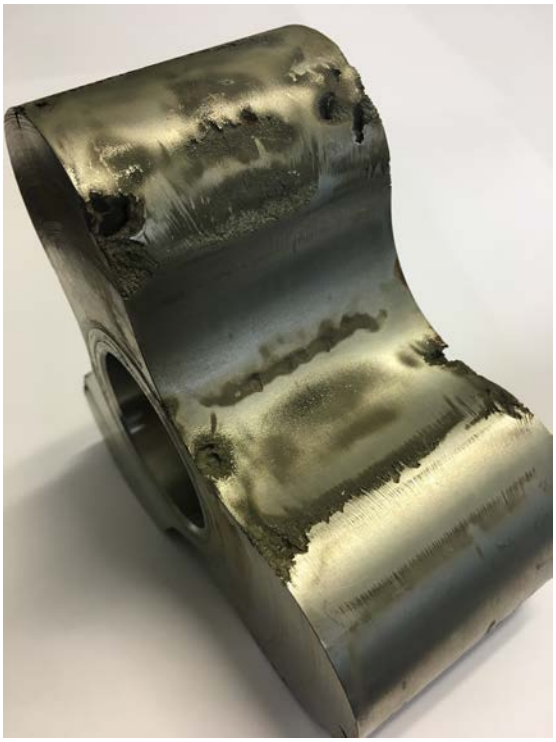

Figure 6: Cavitation erosion damage in a gear pump. The characteristic "orange peel" appearance is observed in the less eroded regions, whereas mass loss and material removal are observed in the most severely eroded regions (LEGI mercury cavitation tunnel).

If the bubble collapses under a constant pressure p_∞, this equation can be integrated and the following bubble wall velocity is obtained:

$$\dot{R} = -\sqrt{\frac{2}{3}\frac{p_\infty - p_v}{\rho}\left(\frac{R_0^3}{R^3} - 1\right)} \tag{0.3}$$

In this equation, R_0 denotes the initial bubble radius prior to collapse. Equation (0.3) shows that the velocity of the bubble wall may reach very high values since it goes to infinity when the radius goes to zero. In reality, bubble wall remains obviously finite because of several effects not taken into account in this simplified approach such as compressibility and non-condensable gases that become predominant at the very end of collapse.

Still on the basis of equation (0.2), it can be shown [13] that the maximum pressure p_{max} generated in the liquid close to the bubble wall is given by:

$$\frac{p_{max} - p_\infty}{p_\infty - p_v} \cong \frac{1}{4^{4/3}}\left(\frac{R_0}{R}\right)^3 \tag{0.4}$$

This equation is valid when the bubble has significantly collapsed i.e. for $R << R_0$. It shows that, together with high velocities, high pressures are generated during collapse since the model predicts that p_{max} goes to infinity at the end of collapse ($R \to 0$). As an example, when a cavitation bubble collapses in water ($p_v = 2300\ Pa$) under an applied pressure $p_\infty = 1\ atm = 10^5\ Pa$ and reaches a radius 50 times smaller than its initial radius ($R_0 / R = 50$), the maximum pressure estimated from Equation (0.4) is $p_{max} = 1.9\ GPa$, which is beyond yield stress and ultimate strength of conventional alloys. Even if this estimate is questionable because of oversimplifying assumptions, it clearly indicates that the collapse of a cavitation bubble may generate impact loads of high amplitude that are likely to damage neighboring walls as revealed in 1917 by Rayleigh [14].

Another important order of magnitude that can be derived from Equation (0.3) is the collapse time or bubble lifetime. It is given by [13]:

$$\tau = 0.915 R_0 \sqrt{\frac{\rho}{p_\infty - p_v}} \tag{0.5}$$

In the same conditions as previously ($p_\infty = 10^5 Pa$, $p_v = 2300\ Pa$, $\rho = 1000\ kg/m^3$) and for a bubble of initial radius $R_0 = 1\ mm$, the collapse time is $\tau = 92\ \mu s$. This estimate shows that the lifetime of a cavitation bubble is generally quite small, which is consistent with the high collapse velocities mentioned above. Thus, the high impact load generated by the collapse of a cavitation bubble has a short duration that is actually smaller than the bubble lifetime estimated here and typically of the order of a few microseconds or even less. This means that the loading is strongly unsteady and that the material should be characterized at high strain rate (see Section 6).

It should be also observed that the impact load is applied on a small surface that scales with the bubble radius and that is actually significantly smaller than the initial bubble radius, typically measured in micrometers. In conclusion, the loading conditions due to cavitation are very peculiar since they are the result of a series of impact loads of high amplitude, small duration and small size randomly distributed over the surface.

The physics of cavitation bubble collapse is however much more complicated than the simple Rayleigh model given by Equation (0.2) could suggest. Because of the vicinity of the wall, spherical symmetry is obviously broken and the bubble does not remain spherical when collapsing. A careful observation of some bubbles in Figure 1 shows that the upper part of the bubble wall sinks into the bubble during collapse. This is the signature of a liquid microjet that develops towards the wall and hits the wall after piercing the whole bubble that finally becomes a toroidal bubble. Computations [7] have shown that the microjet velocity V_j scales with $\sqrt{(p_\infty - p_v)/\rho}$, which is the order of magnitude of the bubble wall velocity given by the previous spherical model (Equation (0.3)). The pressure on the wall due to the impact of the microjet can be estimated from the conventional water hammer formula:

$$\Delta p = \rho c V_j \tag{0.6}$$

where ρc is the acoustic impedance of the liquid (ρ : density, c : speed of sound). Typical values of the microjet velocity are a few hundred meters per second [7]. In the case of water ($\rho = 1000\ kg/m^3$, $c = 1500\ m/s$) and for a typical microjet velocity $V_j = 250\ m/s$, the impact pressure given by Equation (0.6) is $\Delta p = 0.4\ GPa$. This order of magnitude confirms that high impact loads are generated during bubble collapse.

In addition to the potential damaging effect of the microjet, the collapse of a bubble generates shock waves that can also damage the wall. The formation of shock waves during bubble collapse has been widely analyzed from both experimental and numerical approaches (see e.g. [15-21]). There are several reasons for the formation of shock waves during bubble collapse. One is connected to non-condensable gases that a cavitation bubble usually contains, in addition to the liquid vapor. In the case of water, it may be nitrogen and oxygen from the air that are dissolved into water and diffuse through the bubble interface. Non-condensable gases are highly compressed during the final stage of collapse so that a high pressure, and incidentally a high temperature, is reached at the end of collapse. This high pressure forces the bubble to rebound and gives rise to a shock-wave propagating outwards during the rebound phase that follows the collapse. A shock wave is also produced when the microjet perforates the bubble and hits the opposite liquid-vapor interface [7]. Whatever may be their origin, it is widely agreed that shock waves are formed during bubble collapse and that they may contribute to damage neighboring walls together with the microjet.

Although the present section has focused on single bubble collapse, a cavitating flow generates a very large number of bubbles that may interact with each other so that the collapse of a given cavitation bubble in the cloud may be different from what it would be if the bubble were isolated. This is particularly the case for cloud cavitation (see Figure 3) that is known to have a high erosive potential [22]. As an example, Wang and Brennen [23] have shown that, when the bubble interaction effects are

dominant in a bubble cloud, the collapse of the cloud results in the formation of a shock wave that propagates inward and strengthens because of geometric focusing, resulting in an enhanced damage potential.

In addition, we should also mention than other types of vapor structures such as cavitating vortices or vortex cloud cavities may prove to be more aggressive than spherical bubbles when collapsing [24-26].

3 Laboratory testing methods

Several types of laboratory devices have been developed in order to evaluate the resistance to cavitation erosion of materials among which rotating disks, vibratory devices, cavitating liquid jets and high-speed cavitation tunnels. A detailed review of laboratory testing methods is available in [7]. A short description of each of these devices is given below.

Rotating disk devices are made of a water chamber in which a disk is rotating [27-29]. Cavitators such as holes or protruding pins are used in order to induce cavitation. Specimens to be eroded may be mounted on the rotating disk close to the cavitators or on a stationary disk facing the rotating disk. Specimens are generally weighted in order to measure mass loss and rank the tested materials according to their resistance to cavitation.

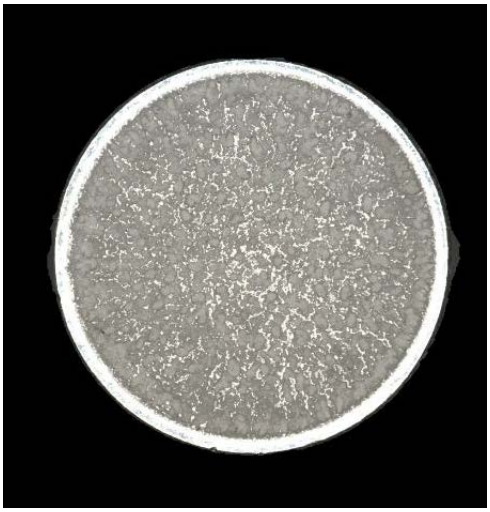

(a)

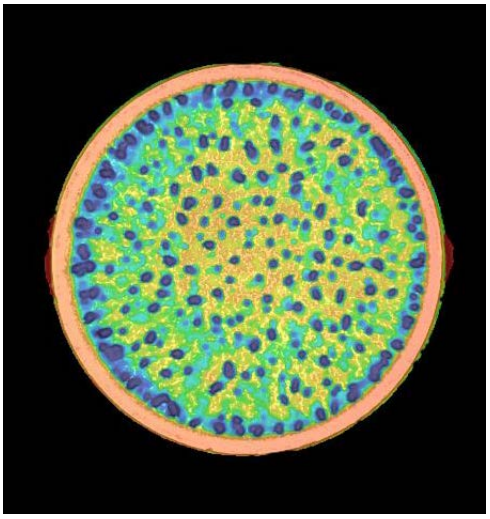

(b)

Figure 7: Typical erosion pattern obtained with a vibratory device. The eroded tip is made of 18-8 stainless steel. Exposure time is 10 hours. Tip diameter is 16 mm as specified in the ASTM standard. Liquid is deionized water at 25 °C. Horn frequency is 19.5 kHz and peak to peak displacement amplitude is 50 µm. (a) Picture of the eroded vibrating tip. (b) Analyzed 3D profile (red: shallow, blue: deep) (Courtesy of Prof. Shuji Hattori, Fukui University).

In vibratory devices, cavitation is produced by the vibration at high frequency of the tip of an ultrasonic horn in a small water reservoir of typically a few liters. It is a standard test method for cavitation erosion known as ASTM G32. Vibration frequency is typically 20 kHz and peak-to-peak displacement of the horn tip 50 µm. Pressure at the horn tip varies periodically and for these typical operating conditions, the pressure amplitude is such that negative pressures periodically occur, which generates cavitation bubbles. The specimen to be eroded may be mounted at the horn tip itself (direct method) or may be stationary and placed at a small distance below the horn tip (alternative method). The erosion patterns obtained by the two methods are significantly different and mass loss by the direct method is generally larger than that of the alternative method. A typical erosion pattern obtained with a vibratory device is shown in Figure 7.

Cavitating liquid jets may also be used to estimate the resistance of materials to cavitation erosion according to standard G134 or its variants. In that case, cavitation is of shear type. A high-speed water jet is produced by a plunger pump at a high pressure that is typically of the order of several tens or possibly hundreds of MPa. The jet is generated through a millimeter-sized nozzle whose detailed

design may be optimized to increase flow aggressiveness and reduce test duration [7, 30]. The jet is discharged in a water cell where the ambient pressure can be changed to control the extent of cavitation if needed. Cavitation structures are caused by the high shear between the jet and the almost still water of the discharge cell. The specimen to be tested is mounted perpendicularly to the jet at a typical distance of a few centimeters. Figure 8 shows typical views of a cavitating jet and an eroded specimen. Like in many other cavitation erosion devices, water temperature needs to be controlled in order to limit temperature rise.

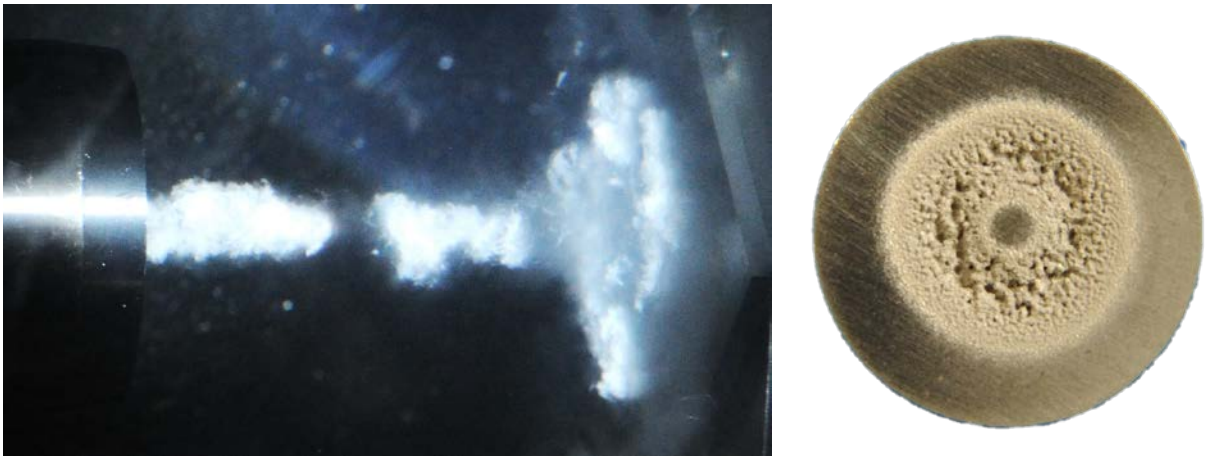

(a) *(b)*

Figure 8: Cavitating jet device. (a) Snapshot of the cavitating jet. Nozzle is on the left and specimen on the right. Injection pressure 30 MPa, nozzle diameter 2 mm, cavitation number 0.014. (b) Typical view of an eroded specimen: stainless steel SUS316L, injection pressure 20 MPa, cavitation number 0.014, exposure time 350 min (Courtesy of Prof. Hitoshi Soyama, Tohoku University).

The behavior of materials in a cavitation field can also be investigated in the laboratory using a high-speed cavitation tunnel. A high flow velocity is required in the test section in order to achieve significant damage within reasonable exposure times. Indeed, cavitation aggressiveness increases with flow velocity in a very non-linear way, as a power law with an exponent typically of the order of 4 to 9. Several types of test sections have been designed for cavitation erosion testing such as Venturis [31, 32] and test sections with various types of cavitators [33, 34]. A radially diverging test section [35] is shown in Figure 9 together with a typical erosion pattern obtained using this special design. One of the main advantages of high-speed cavitation tunnels is that they produce a hydrodynamic type cavitation,

which is generally more representative of industrial applications than vibratory devices. On the other hand, vibratory devices are much smaller and easy to operate.

(a) *(b)*

Figure 9: Example of a cavitation erosion tunnel using a radially diverging asisymmetric test section. (a) Visualization of the attached cavity. Nozzle diameter is 16 mm. (b) Typical example of an eroded specimen. Erosion is concentrated on a ring that corresponds to the closure region of the cavity shown in (a). Specimen diameter: 100 mm (LEGI Prevero facility).

Laboratory testing devices have been extensively used in order to characterize the resistance of various materials to cavitation erosion. As an example let us mention the work of Hattori et al. [36-38] (also presented in [7]) who constructed a database for 143 materials including various types of metallic alloys as well as plastics and ceramics. Erosion resistance, defined as the inverse of the erosion rate (in µm/h), was measured under various operating conditions using vibratory and liquid jet devices. Maximum erosion rate was generally considered since the erosion rate progressively increases at the beginning of the test and also may not tend to a strictly constant value for large exposure times (see Section 0). The authors have shown that for each class of alloy (such as carbon steels, aluminum alloys, titanium alloys…), the erosion resistance can be estimated in a relatively reliable way from material hardness (see e.g. Figure 10 for carbon steels). A major limitation of such a correlative technique is that the correlation generally differs from one class of material to another. Whatever may be the mechanical property (such as hardness, strain energy, ultimate resilience or others) that is used to correlate with erosion resistance, it appears that the correlation is far from being universal [39].

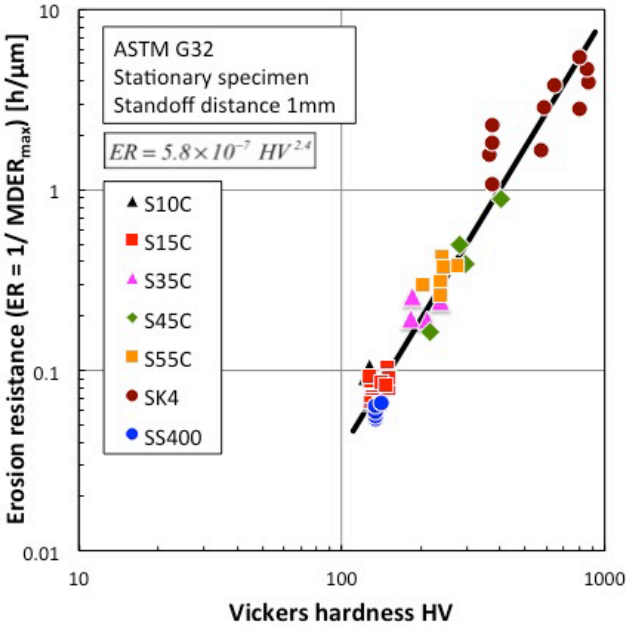

Figure 10: Correlation between hardness and erosion resistance for carbon steels as measured with the ASTM G32 vibrating device (Hattori et al. [36]).

It should be observed that erosion tests in the laboratory should reproduce as much as possible the real conditions of the industrial case under consideration in order to guarantee reliability of the prediction. This includes cavitation pattern and development but also flow aggressiveness. In particular, cavitation aggressiveness in the laboratory should be representative of the real case. This condition is not necessarily fulfilled since the operating conditions of laboratory testing devices are often chosen to accelerate damage and minimize test duration rather than to reproduce the actual aggressiveness. This may be a difficulty for certain materials such as polymers [40] that may exhibit very limited erosion below a given threshold and a dramatic deterioration above it. It is however still an open question to what extent laboratory tests are representative of real cavitating conditions such as in a marine propeller or hydraulic turbine.

4 Pitting and the incubation period

Pitting is typical of the earlier stage of cavitation erosion known as the incubation period during which no significant mass loss occurs. During this initial stage, damage is characterized by isolated indents on the material surface as shown in Figure 11. Each pit is supposed to be the result of a single bubble

collapse. When increasing the exposure time, pit density obviously increases and more and more overlapping occurs. This leads to the so-called orange peel structure of the surface. Since individual pits are very shallow surface depressions, they can be observed only if the material surface was finely polished prior to testing. In the case of stainless steel 316 L eroded by a water cavitating flow, pit diameter typically ranges from a few micrometers to a few hundred of micrometers whereas pit depth is of the order of a few percent of pit diameter or less [41]. Although pitting is more especially observed on ductile metallic alloys that deform plastically under the action of bubble collapse, pits can also be formed in other materials such as polymers [40].

Figure 11: Typical cavitation erosion damage during the incubation period. Damage is characterized by nearly isolated pits. The image results from profilometry measurements using a contact profilometer with a measuring step of 1 µm in both horizontal directions. The image was distorted vertically in order to make pits more visible. Specimen eroded in the LEGI cavitation erosion tunnel (see Figure 9), stainless steel 316L, image size 2 mm × 4 mm [35].

The interest of pitting tests essentially lies in the fact that it is a good way to characterize cavitation aggressiveness also called in the literature cavitation intensity. Cavitation aggressiveness can be estimated from histograms of pit size as shown in Figure 12 where pitting rate per unit surface area and unit exposure time has been plotted as a function of pit diameter. Generally, cumulative pitting

rate N follows an approximately exponential law with pit diameter D that can be expressed by the following equation [7]:

$$N = \frac{8}{\pi \delta^2 \tau} e^{-\frac{2D}{\delta}} \tag{0.7}$$

In this equation, δ is a characteristic pit diameter and τ a characteristic time that are both reviewed hereafter.

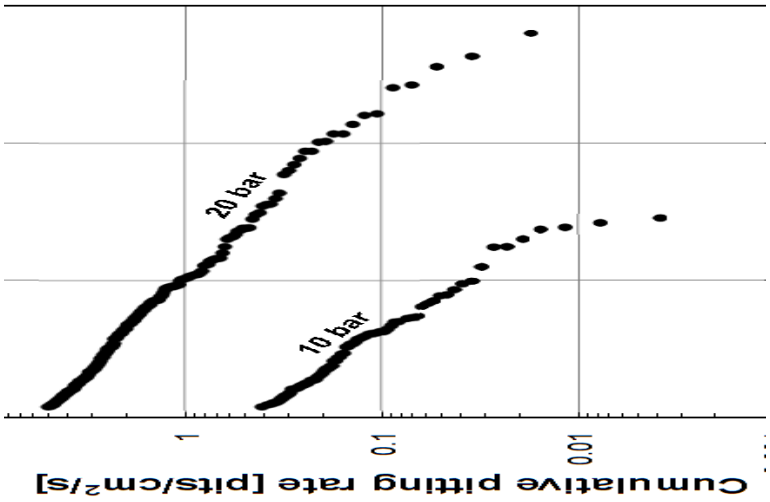

Figure 12: Typical histograms of pitting rate. Material is stainless steel A2205. The specimen was eroded in the LEGI cavitation erosion tunnel. Pitting test results for two different operating conditions corresponding to two different values of the upstream pressure are shown (10 bar and 20 bar). Cavitation number was kept constant and equal to 0.9 so that the effect presented in Figure 12 is a purely velocity effect [42].

Although smaller pits are very numerous, it can be shown [7] that they tend to not contribute significantly to the eroded surface because of their small size. The same conclusion holds for larger pits that also tend to not contribute significantly to the eroded surface, but for a different reason which is because of their small density. As a result, there is an intermediate class of pit diameters whose contribution to the eroded surface is maximum. This class is centered on parameter δ introduced

above which consequently appears as an important characteristic pit size with respect to cavitation erosion damage.

Regarding the characteristic time τ introduced in Equation (0.7), it can be interpreted as the coverage time, i.e. the time required for the surface of the wall to be fully covered exactly once by pits [7]. It is a characteristic time of the erosion process, together with the incubation time presented in Section 5, whose importance is emphasized in Section 6.

An increase in flow velocity generally induces both an increase in pitting rate and an increase in pit size. This is qualitatively visible in Figure 12 where two histograms corresponding to two different operating pressures or flow velocities have been plotted. Since pit diameter scales with parameter δ and pitting rate with $1/(\delta^2\tau)$ as shown by Equation (0.7), the influence of operating conditions such as flow velocity on flow aggressiveness can be reduced to its influence on both parameters δ and $1/(\delta^2\tau)$. From data presented in Figure 12, it can be shown [42] that the characteristic pit diameter δ increases with flow velocity V as $V^{0.75}$ whereas the characteristic pitting rate $1/(\delta^2\tau)$ increases much more rapidly, typically as V^5. As a result, the coverage time τ decreases quite rapidly with flow velocity as $V^{-6.5}$. Although these results are geometry dependent, they clearly demonstrate the strongly non-linear effect of flow velocity on cavitation aggressiveness.

Another way to characterize flow aggressiveness is to measure the pressure pulses due to bubble collapse using pressure sensors flush mounted on the wall [43-47]. Figure 13 presents a typical signal given by a pressure sensor in a cavitating flow. The signal is made of a series of pressure pulses of small duration and variable amplitude. An increase in flow velocity generally results in an increase in both pulse rate and pulse amplitude [7]. Each pressure pulse is expected to be due to the collapse of a single bubble. If the amplitude is larger than the material yield stress, a plastic deformation or pit is expected. Thus, there is a great similarity between pitting tests and pressure pulse measurements. In

some way, the material used for pitting tests can be considered as a particular pressure sensor whose detection threshold is the yield stress.

Pressure pulse measurements using conventional pressure sensors are often difficult to perform because of the extreme features in amplitude (Δ GPa), duration (Δ μs) and radial extent (μm) of the pulses. Pressure sensors of high performances particularly in frequency response with in addition a high mechanical resistance in order not to be damaged by cavitation are then required. It is not straightforward to estimate the actual stress applied to the material because of the usually large discrepancy between the area of the sensor sensitive surface (usually Δ mm) and that of the cavitation impact load (Δ μm). Despite these difficulties, pressure pulse measurements are, together with pitting tests, a good way to characterize the aggressiveness of a cavitating flow. Both techniques are complementary since the time dependency of impact loads is available from pressure pulse measurements only and the radial extent of impact loads from pitting tests only. A technique based on FEM simulations is presented in Section 8 to derive impact load amplitudes from pitting tests.

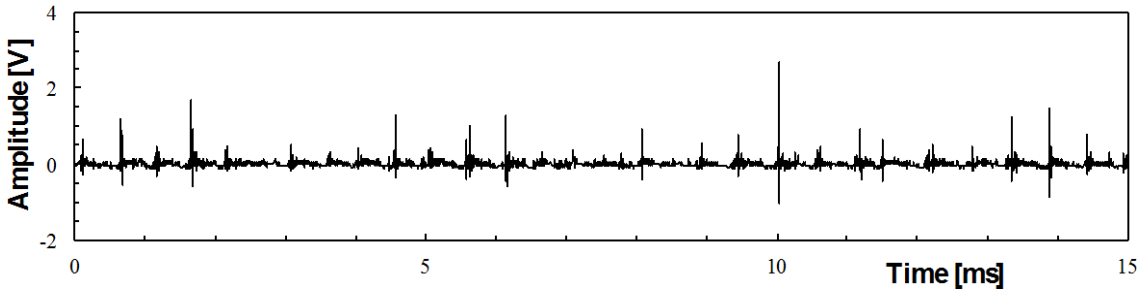

Figure 13: Typical signal measured by a pressure sensor in a cavitating flow. The amplitude is here expressed in Volt. Since the sensitive area of the pressure sensor is much larger than the size of the impact loads, it is not straightforward to convert the amplitude into pressure units [43].

5 Mass loss and the advanced periods of erosion

During the incubation period i.e. for relatively small exposure times (see Section 4), cavitation damage in metals is mostly characterized by plastic deformations. Although the most intense impacts may lead to rupture, material removal remains confined to a microscopic scale and mass loss is insignificant at a macroscopic level during the incubation period. This regime of zero mass loss occurs for an initial

period of time which is known as the incubation time and which is an essential characteristic time of the erosion process, together with the coverage time defined in Section 4. The relationship between both characteristic times is discussed in Section 6.

The incubation period is followed by an acceleration period during which mass loss progressively increases as shown in Figure 14. During the acceleration period, the erosion rate, defined as the time derivative of mass loss, grows from zero to generally a constant value that characterizes the steady-state regime of erosion. The eventual erosion rate is a key parameter in cavitation erosion. Erosion resistance is often defined as the inverse of the eventual erosion rate (cf. Section 3).

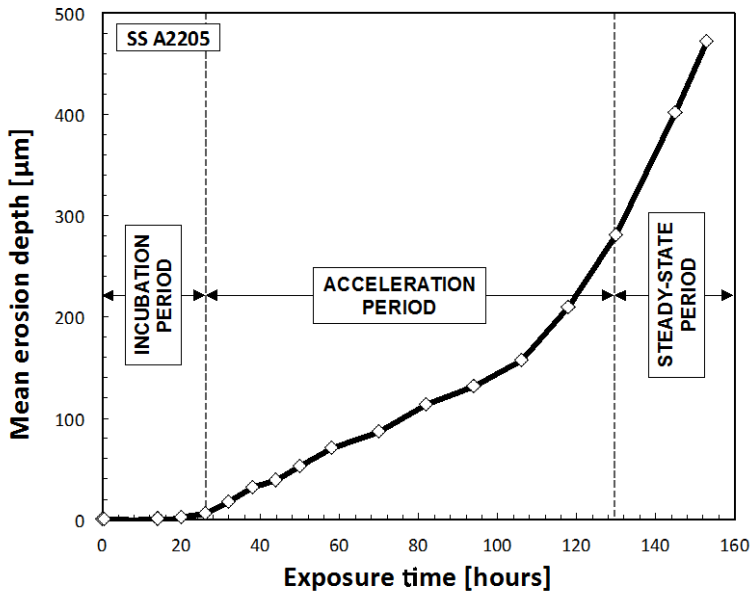

Figure 14: Typical mass loss curve showing the incubation period, the acceleration period and the steady-state period. The incubation period is characterized by a negligible mass loss whereas the steady-state period is characterized by a constant slope measuring the erosion rate (same operating conditions as in Figure 15).

More complicated evolutions of mass loss with exposure time may be observed. They are mainly due to changes in wall geometry caused by erosion, which, in turn, affect the cavitating flow. Among these changes, let us mention the change in roughness that may locally affect bubble collapse, and the erosion of the wall itself that obviously changes the flow geometry and consequently its aggressiveness. Several analytical expressions have been proposed in order to approximate mass loss curves, among which Gaussian and/or power laws [7].

Figure 15 presents mass loss curves for three different metallic alloys. It can be observed that the smaller the incubation time, the larger the steady-state erosion rate. Correlations have been proposed between the erosion rate $\dot{e}$ (typically measured in µm/h) and the incubation time T in the form:

$$\dot{e} = k\left[\frac{1}{T}\right]^{\alpha} \tag{0.8}$$

with an exponent α of the order of unity [35, 48, 49]. Such a relationship makes it possible to estimate the eventual erosion rate from the incubation time. A further discussion of this correlation is available in [7].

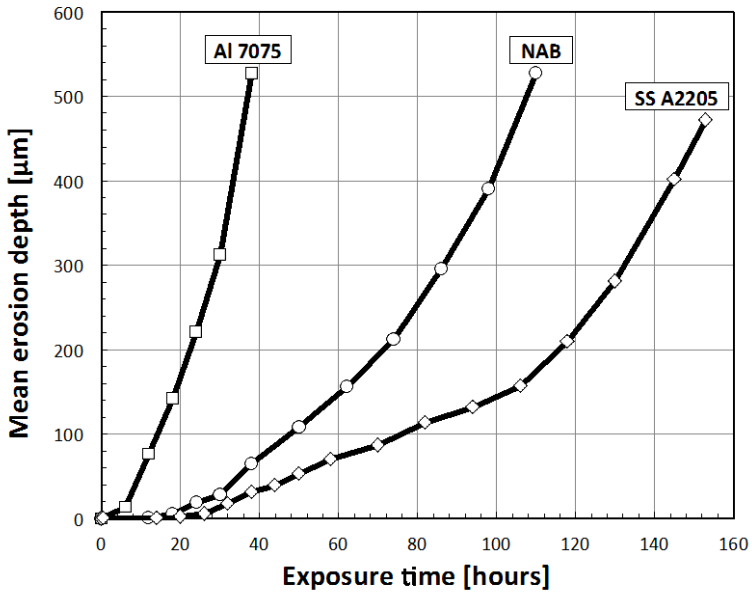

Figure 15: Mass loss curves for three different metallic alloys: aluminum alloy 7075, nickel aluminum bronze alloy C95400 and duplex stainless steel A2205. Mass loss tests were conducted in the LEGI cavitation erosion tunnel (see Figure 9). Upstream pressure 40 bar, cavitation number 0.9.

Cavitation erosion damage is usually not uniform over the whole surface of the wall subjected to cavitation as shown in Figure 16. This is due to the spatial distribution of flow aggressiveness which is not uniform. In the case of an attached cavity as shown in Figure 3, which is also the case for the erosion presented in Figure 16 (see Figure 9a), maximum erosion occurs in the region of closure of the cavity since it is the region where most cavitation bubbles collapse. When moving upstream or

downstream from cavity closure, flow aggressiveness decreases and cavitation erosion damage decreases too. This is the reason why a maximum in the depth of erosion is observed in Figure 16.

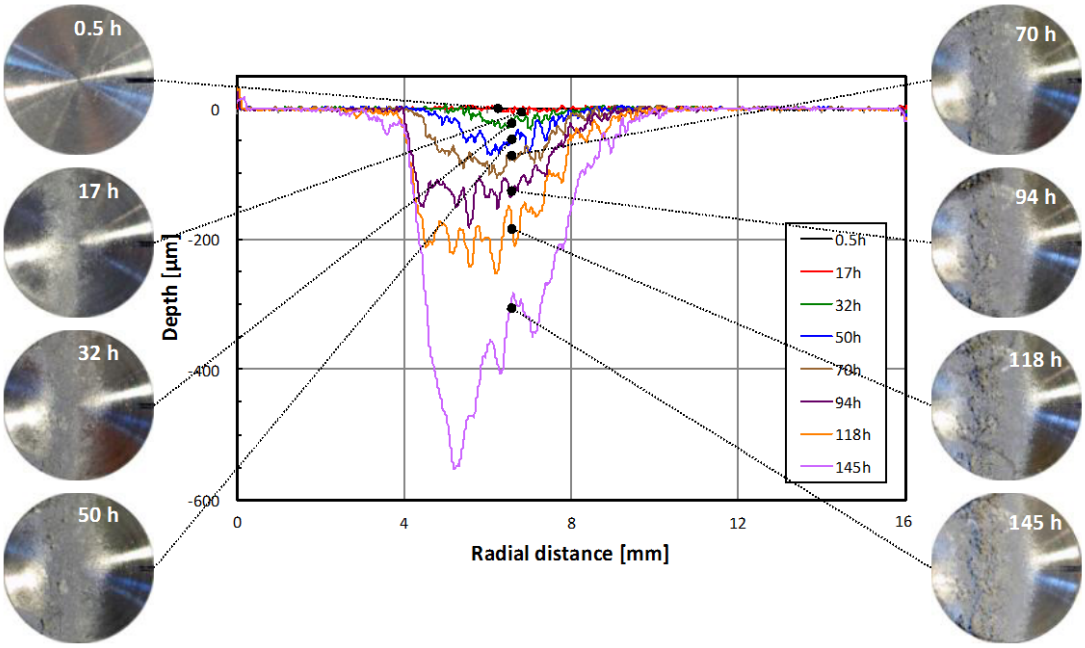

Figure 16: Typical example of the erosion of a sample in a cavitation tunnel and associated profiles of erosion as a function of exposure time. Stainless steel A2205, upstream pressure 40 bar, cavitation number 0.9. Specimen eroded in the LEGI cavitation erosion tunnel (see Figure 9).

6 Material selection and surface protection to prevent cavitation erosion

Different options are available in order to improve the resistance to cavitation erosion. The first option is to select a material with a large capability to sustain the propagation of a crack (defined by the fracture toughness K_{Ic}) and an important yield stress σ_y in order to prevent plastic deformation. Another important parameter is the fatigue stress corresponding to the maximum stress amplitude the material could sustain for a given number of cycles. Figure 17 shows a typical plot of the fracture toughness versus the fatigue strength for metals. The objective being to maximize the performance index K_{Ic}/σ, best materials are located on the upper-right part of the graph where stainless steels and low alloy steels are indicated.

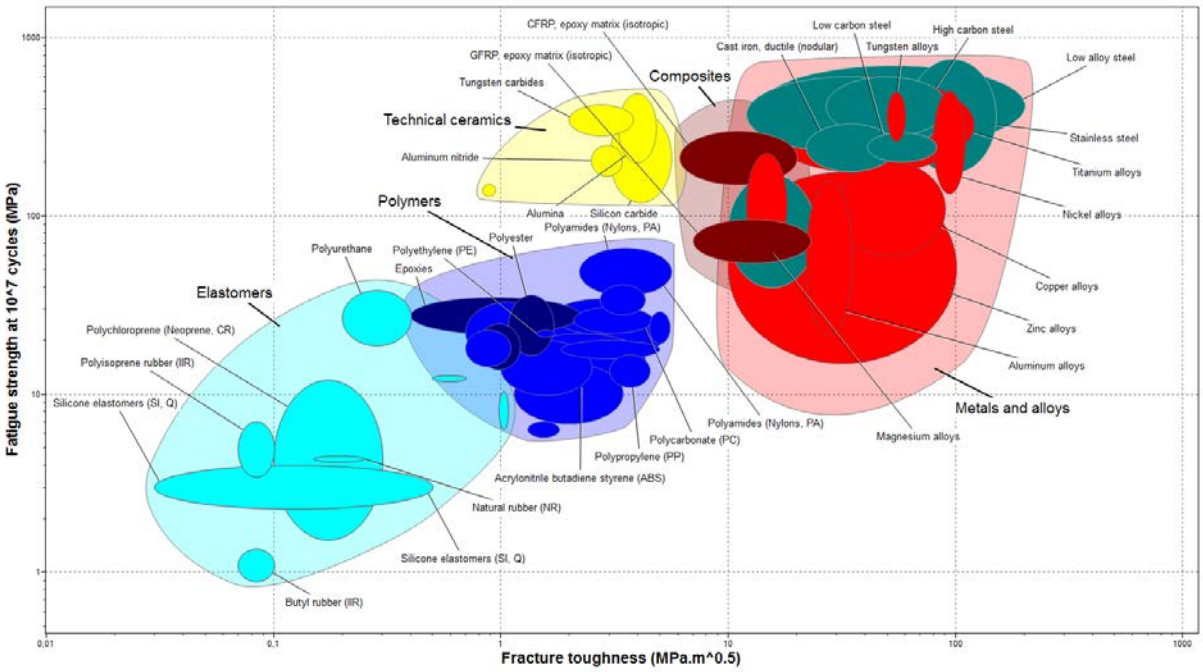

Figure 17: Ashby map of materials represented by their fatigue strength at 10^7 cycles and fracture toughness [50].

Such a basic selection algorithm explains why stainless and duplex steels are commonly used for propellers and fuel injectors. Figure 17 also shows that nickel alloys are good candidates for cavitation erosion resistant materials. Some recent papers proved that adding Mo in AISI 316L improved the cavitation erosion resistance of this specific stainless steel [51].

Since cavitation erosion starts at the surface of the material, another solution consists in applying a surface treatment that could delay the crack nucleation [52]. Here again the objective is to enhance the fracture toughness and the hardness (which is closely related to the yield stress) but only close to the surface. This could be done for example by pre-deforming the surface by shot peening. The key idea is to take advantage of the material hardening in order to increase locally the yield stress. This induces a compressive stress at the surface which prevents crack opening and consequently increases the fatigue life [53].

An alternative to mechanical surface treatment is the deposition of a layer coating on the surface exposed to cavitation erosion. Such a technology is commonly used in applications to extreme

environments like high temperature or oxidation medium. As an example, TiN coatings deposited by Plasma Vapor Deposition (PVD) method or by cathodic arc method strongly increases the hardness of the substrate (up to 25 GPa to be compared to an average 5 GPa hardness of stainless steels) and have been tested in cavitation erosion [54]. Mechanical properties can be further improved when the coating is made of nanocristals [55]. Although promising, one should be able to overcome two major difficulties in order to transfer this technology to cavitation erosion problematics. Firstly, the coating thickness is usually very small and brittle, so that it needs to be designed a-priori in order to sustain the highest load possibly experienced during the cavitation exposure. Secondly, the adherence between the coating layer and the substrate is a weak point which could be catastrophic in the case of delamination [56-58].

Another option could be based on the capability of the material to dissipate energy while remaining in the elastic domain. In that sense, polymers are very good candidates [40, 59-64]. As an example, cavitation erosion tests performed on various densities of Ultra High Molecular Weight Polyethylene (UHMWPE) coatings have demonstrated outstanding resistance to cavitation erosion [40]. The key issue for polymer coating technology regards the adhesion with the substrate. An alternative choice consists in using amorphous metals which exhibit a very high yield stress and thermoplastic forming ability. As an example, Zr based Bulk Metallic Glasses (BMGs) showed high resistance to erosion and corrosion compared to conventional 304L stainless steels which were attributed to the absence of grain boundaries in the metal [65, 66]. For such BMGs, the incubation time was measured to be approximately 10 times higher than that of 304L austenitic stainless steels.

7 Material response to cavitation impact loads

In order to analyze the response of a given material to cavitation, its properties and more especially its stress-strain relationship should be determined. This is an essential input particularly when the material response is computed using a Finite Element Method (FEM) approach such as presented in Section 8.

The stress-strain relationship can be determined from conventional quasi-static tensile or compression tests. For cavitation applications, it may be however preferable to use a testing technique that is more representative of cavitation pitting. This is the case of nanoindentation tests that proved to be more appropriate to cavitation because of their confined nature and because of the similarity between a nanoindentation imprint and a cavitation pit. For some materials and depending upon the distribution and size of inclusions, a significant difference may exist between the global and the local behavior of the material. The latter that is derived from nanoindentation tests should be preferred in cavitation erosion [67].

As mentioned in Section 2, the impact load due to the collapse of a cavitation bubble is of small duration so that the expected strain rate is high. Material properties should then be characterized at high strain rate. For a rough estimate of strain rate, it can be assumed that the collapse of a cavitation bubble induces a plastic strain in the material of a few percent [7] during a lapse of time of a few microseconds. Then, the resulting strain rate $\dot{\varepsilon}$ is of the order of $10^{-2}/(10^{-6}s) \approx 10^{4}s^{-1}$. Recent studies have shown that strain rate in cavitation pitting may even be one or two orders of magnitude larger [68]. In order to account for the effect of strain rate, nanoindentation tests generally conducted at a small strain rate should be complemented by specific tests such as Split Hopkinson Pressure Bar (SHPB) tests. SHPB tests allow an estimation of the strain rate sensitivity [67] that can be included in FEM simulations using a model such as the Johnson-Cook plasticity model in which a logarithmic dependency of flow stress with strain rate is assumed.

Cavitation bubble collapses induce a surface hardening of the material comparable to that obtained in conventional peening [69, 70]. As a result, when a metallic alloy is subjected to cavitation, the most superficial layers are hardened. Figure 17 presents a typical example of micro-hardness profiles measured in cross sections of specimens eroded by cavitation. The strain profile within the material can usually be modeled by the following power law:

$$\varepsilon(x) = \varepsilon_0 \left(1 - \frac{x}{L}\right)^{\theta} \tag{0.9}$$

where $\varepsilon(x)$ is the strain at depth x from the eroded surface and ε_0 the strain on the eroded surface that is often considered as the rupture strain since failure has been reached on the eroded surface [7, 35]. L is the thickness of the hardened layer and θ is the shape factor of the power law. A phenomenological model of cavitation erosion presented in [7, 71] shows that the erosion rate is proportional to the ratio L/τ where τ is the coverage time introduced in Section 4. The ratio L/τ has the dimensions of an erosion rate (typically in µm/h) and can be considered, according to this model, as a relevant order of magnitude of the erosion rate [7]. This characteristic erosion rate depends upon both metallurgical and hydrodynamic parameters via the two factors L and τ. Moreover, the model predicts that the incubation time is proportional to the coverage time [7]. Hence, the thickness of the hardened layer L and the coverage time τ appear respectively as a relevant length scale and a relevant time scale of the cavitation erosion phenomenon from which a relevant erosion rate can be computed.

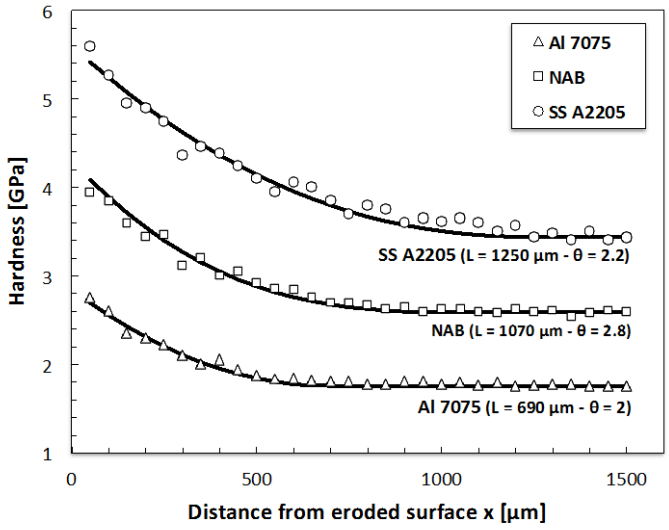

Figure 18: Micro-hardness profiles in eroded samples for three different metallic alloys: aluminum alloy 7075, nickel aluminum bronze alloy C95400 and duplex stainless steel A2205. Mass loss tests were conducted in the LEGI cavitation erosion tunnel (see Figure 9). Upstream pressure 40 bar, cavitation number 0.9. Solid lines correspond to Equation (0.9) where the two parameters L and θ have been determined from a best fit procedure.

8 Fluid/structure interaction

The fluid/structure interaction plays a role in cavitation erosion particularly for compliant materials. If the wall is not perfectly rigid, its deformation during impact contributes to damping the amplitude of the hydrodynamic impact. This effect was measured by Hattori et al. [64] in the case of plastics and can be approached, in a simplified way, by considering a high-speed liquid jet hitting normally an elastic solid.

According to this model, the impact pressure Δp is given by the following equation [13]:

$$\Delta p = \frac{(\rho c)_\ell V_j}{1 + \dfrac{(\rho c)_\ell}{(\rho c)_s}} \tag{0.10}$$

where ρc is the acoustic impedance of either the liquid (index ℓ) or the solid (index s) and V_j the velocity of the impacting liquid jet that simulates the microjet formed during bubble collapse (see Section 2). In the case of a rigid wall, the acoustic impedance of the solid tends to infinity and Equation (0.10) reduces to $\Delta p = (\rho c)_\ell V_j$ which is the same as the water hammer equation (0.6).

Equation (0.10) shows that the fluid structure interaction is controlled by the ratio of the acoustic impedance of the liquid to that of the solid $\alpha = (\rho c)_\ell / (\rho c)_s$. The influence of parameter α on the impact pressure given by Equation (0.10) is shown in Figure 18 together with a few typical values of α for different liquid/solid systems. In the case of water and aluminum, the impact pressure is reduced by about 10% in comparison to the perfectly rigid case whereas the reduction is expected to be much more important in the case of mercury and aluminum of the order of 60%. This damping effect may also be quite important in the case of water and soft coatings.

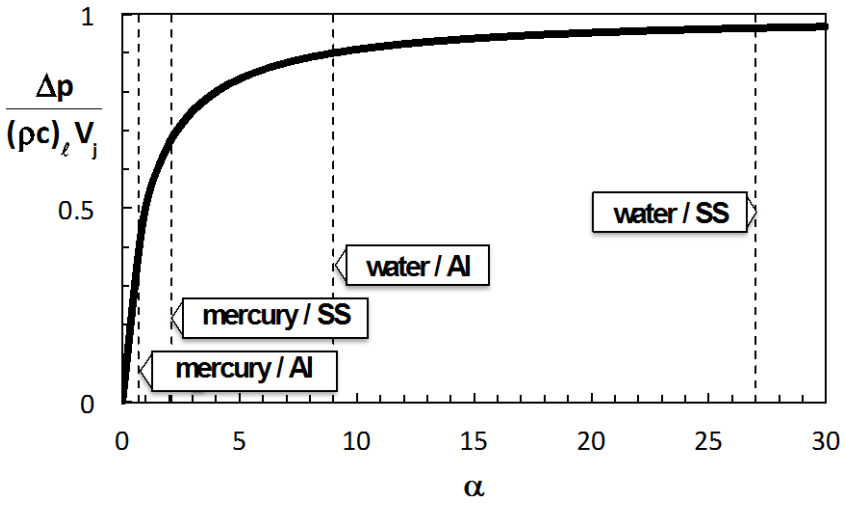

Figure 19: Influence of the elasticity of the wall on the impact pressure of a high-speed liquid jet.

The fluid/structure interaction in cavitation erosion can also be approached numerically by coupling a fluid dynamics code to a solid mechanics code. Up to now, the coupling has been done in the case of a single bubble collapsing in the vicinity of a wall [7]. In order to approach the actual pressure distribution on the wall partly due to shock waves generated during bubble collapse, liquid compressibility should be included in the CFD (Computational Fluid Dynamics) code. As for the solid code, dynamic simulations should be done in order to account for dynamic effects using a plasticity model that includes the effect of strain rate such as the Johnson-Cook plasticity model mentioned in Section 6. A one-way coupling may be used by just subjecting the wall to the pressure field deduced from the CFD code or a two-way coupling may be used if the feedback action of the wall deformation on bubble collapse (including the damping effect mentioned above) is looked for.

9 Towards a FEM numerical prediction of cavitation erosion damage

Although empirical correlations between cavitation erosion resistance and material properties (see Section 3) are of great interest in practice, the trend today is to use Finite Element Modeling (FEM) in order to predict the behavior of materials in cavitation environments. As discussed in Section 2, loading conditions due to cavitation are very specific since they are made of successive impact loads of high amplitude, small duration and small radial extent. By properly simulating the response of the

material to such impact loads, it will be possible to predict numerically cavitation erosion damage. Although such simulations are still under development, significant progress reported below has been made in this direction.

FEM simulations can be of great help to determine the aggressiveness of a cavitating flow from pitting tests [68, 72, 73]. In these studies, a synthetic pressure distribution (given for instance by a gaussian law) is assumed for each bubble collapse. The response of the elastic-plastic material to such an impact is computed and particularly the shape of the residual plastic deformation or pit. The technique used in references [68, 72, 73] consists in developing an inverse method in order to compute the characteristics of the pressure distribution from the measured characteristics of the pit. It has been shown [73] that the amplitude in GPa of the impact load responsible for a given pit is directly connected to the pit shape factor defined as the ratio of depth to diameter and that the radial extent of the impact load is proportional to pit diameter. By using this technique for all the pits identified during a pitting test, a distribution of impact loads in the cavitating flow can be determined as a function of their amplitude and size. This distribution is a measure of flow aggressiveness.

The next step that is still under development [74] would consist in computing by a FEM method the response of the material to a series of impacts randomly chosen among the previous distribution and randomly distributed on the material surface. By including a damage model in the FEM simulation, it becomes then possible to predict mass loss. Preliminary results are shown in Figure 19 [75]. 420 cavitation impacts deduced from a pitting test and the above mentioned inverse technique have been simulated on a surface of 500 µm × 500 µm. Mass loss occurs after 360 impacts, which corresponds to the end of the incubation period. The regions where mass loss occurs are surrounded by black lines in Figure 19. The damage model used in this work is based on computations of the cumulated plastic strain. Two critical values of the cumulated plastic strain were introduced corresponding to damage initiation and failure. A damage variable was introduced that is assumed to increase linearly with plastic strain from 0 (undamaged material) to 1 (failure) between the two previous critical values of the cumulated plastic strain. Once failure is reached in a given mesh element, this element is deleted

and its volume contributes to mass loss. Although several issues remain to be solved such as the sensitivity to the computational grid and the choice of the most appropriate damage model for cavitation, such a method opens a new perspective in cavitation erosion prediction.

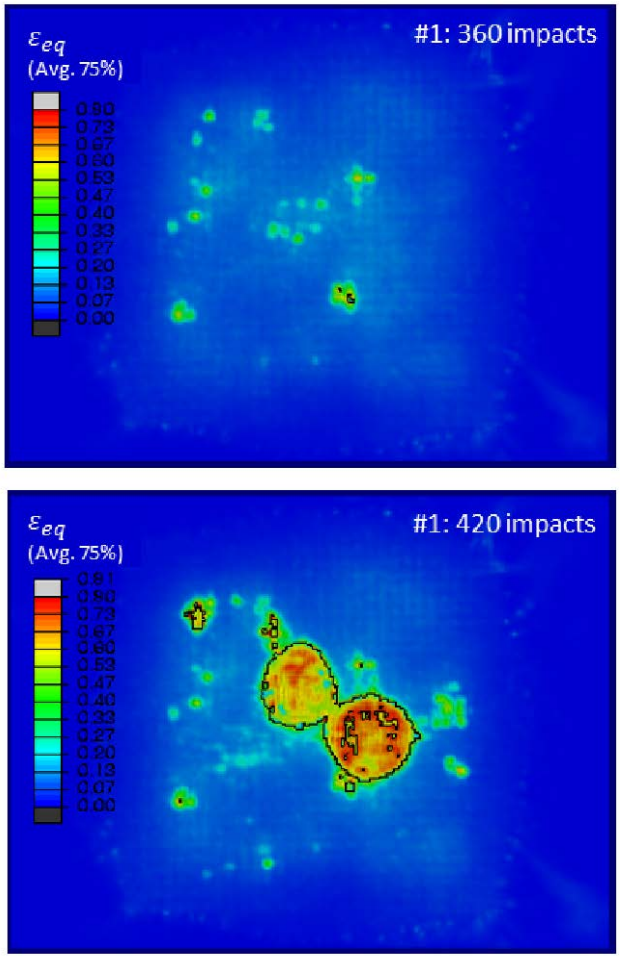

Figure 20: Typical FEM computation of cavitation erosion damage on SS A2205 material. The cavitation aggressiveness was estimated from pitting tests using an inverse FEM computation. Mass-loss started after 360 impacts at some locations. The critical plastic strains at damage initiation and failure were arbitrarily defined as 80% and 90% respectively. Black lines indicate regions where material has been removed [75].

10 Concluding remarks

This paper gives an overview of the state-of-the art of cavitation erosion with a specific focus on the estimation of mass loss. During the past few years, most attention has been paid to simulations of the

cavitation process within the fluid but less studies were oriented towards simulations of the damage induced in the solid and the subsequent mass loss. Recent developments based on FEM calculations appear to be encouraging with respect to cavitation erosion prediction provided two ingredients are made available: (i) the material behavior and (ii) the cavitation loading conditions. The first item implies to characterize the material in testing conditions as close as possible to the conditions imposed by the multiple bubble collapses. This means in particular a confined loading (a few micron in size) applied at a very high strain rate (up to 10^6 s^{-1}). The second item requires to characterize the distribution of impact loads on the material surface due to bubble collapses that usually have extreme amplitudes. In addition, it may be important to account for the fluid structure interaction since the material deformation may damp the hydrodynamic impact loads with respect to a purely rigid wall and/or influence the bubble dynamics itself. To the authors' point of view, such a multiphysic approach, that gives as much importance to the material as it gives to the fluid, sounds very promising as demonstrated by some recent advances in cavitation erosion modeling.

11 References

1. Brennen, C.E., *Cavitation in medicine.* Interface Focus, 2015. **5**(5).

2. Wang, Q., K. Manmi, and K.-K. Liu, *Cell mechanics in biomedical cavitation.* Interface Focus, 2015. **5**(5).

3. Owen, J., P. Rademeyer, D. Chung, Q. Cheng, D. Holroyd, C. Coussios, P. Friend, Q.A. Pankhurst, and E. Stride, *Magnetic targeting of microbubbles against physiologically relevant flow conditions.* Interface Focus, 2015. **5**(5).

4. Chahine, G.L., A. Kapahi, J.-K. Choi, and C.-T. Hsiao, *Modeling of surface cleaning by cavitation bubble dynamics and collapse.* Ultrasonics Sonochemistry, 2016. **29**: p. 528-549.

5. Dular, M., T. Griessler-Bulc, I. Gutierrez-Aguirre, E. Heath, T. Kosjek, A. Krivograd Klemenčič, M. Oder, M. Petkovšek, N. Rački, M. Ravnikar, A. Šarc, B. Širok, M. Zupanc, M. Žitnik, and B. Kompare, *Use of hydrodynamic cavitation in (waste)water treatment.* Ultrasonics Sonochemistry, 2016. **29**: p. 577-588.

6. Loraine, G., G. Chahine, C.-T. Hsiao, J.-K. Choi, and P. Aley, *Disinfection of gram-negative and gram-positive bacteria using DynaJets® hydrodynamic cavitating jets.* Ultrasonics Sonochemistry, 2012. **19**(3): p. 710-717.

7. Kim, K.H., G.L. Chahine, J.-P. Franc, and A. Karimi, *Advanced Experimental and Numerical Techniques for Cavitation Erosion Prediction*. Fluid Mechanics and Its Applications, Vol. 106, ed. R. Moreau. 2013, Dordrecht, Boston, London: Springer.

8. Basumatary, J., M. Nie, and R.J.K. Wood, *The Synergistic Effects of Cavitation Erosion–Corrosion in Ship Propeller Materials.* Journal of Bio- and Tribo-Corrosion, 2015. **1**(2): p. 12.

9. Wood, R.J.K., *Erosion-corrosion interactions and their effect on marine and offshore materials.* Wear, 2006. **261**(9): p. 1012-1023.

10. Wood, R.J.K. and S.P. Hutton, *The synergistic effect of erosion and corrosion: trends in published results.* Wear, 1990. **140**(2): p. 387-394.

11. Wood, R.J.K. and S.A. Fry, *The Synergistic Effect of Cavitation Erosion and Corrosion for Copper and Cupro-Nickel in Seawater*. Journal of Fluids Engineering, 1989. **111**(3): p. 271-277.

12. Brennen, C.E., *Cavitation and Bubble Dynamics*. Oxford Engineering Sciences Series 44. 1995, New York: Oxford University Press.

13. Franc, J.-P. and J.-M. Michel, *Fundamentals of Cavitation*. Fluid Mechanics and Its Applications, ed. R. Moreau. 2004, Dordrecht, Boston, London: Springer.

14. Rayleigh, L., *On the Pressure Developed in a Liquid During the Collapse of a Spherical Cavity*. Philosophical Magazine, series 4, 1917. **34**: p. 94-98.

15. Lauterborn, W. and A. Vogel, *Shock Wave Emission by Laser Generated Bubbles*, in *Bubble Dynamics and Shock Waves*, C.F. Delale, Editor. 2013, Springer Berlin Heidelberg. p. 67-103.

16. Delale, C.F., *Bubble Dynamics and Shock Waves*. 2013: Springer.

17. Ohl, C.D., T. Kurz, R. Geisler, O. Lindau, and W. Lauterborn, *Bubble dynamics, shock waves and sonoluminescence.* Philosophical Transactions of the Royal Society of London A: Mathematical, Physical and Engineering Sciences, 1999. **357**(1751): p. 269-294.

18. van Wijngaarden, L., *Mechanics of collapsing cavitation bubbles.* Ultrasonics Sonochemistry, 2016. **29**: p. 524-527.

19. Tomita, Y. and A. Shima, *Mechanisms of impulsive pressure generation and damage pit formation by bubble collapse.* Journal of Fluid Mechanics, 1986. **169**: p. 535-564.

20. Johnsen, E. and T. Colonius, *Numerical simulations of non-spherical bubble collapse.* Journal of Fluid Mechanics, 2009. **629**: p. 231-262.

21. Fujikawa, S. and T. Akamatsu, *Effects of the non-equilibrium condensation of vapour on the pressure wave produced by the collapse of a bubble in a liquid.* Journal of Fluid Mechanics, 1980. **97**(03): p. 481-512.

22. Bark, G. and R.E. Bensow, *Hydrodynamic mechanisms controlling cavitation erosion.* International Shipbuilding Progress, 2013. **60**: p. 345-374.

23. Wang, Y.-C. and C.E. Brennen, *Numerical Computation of Shock Waves in a Spherical Cloud of Cavitation Bubbles.* Journal of Fluids Engineering, 1999. **121**(4): p. 872-880.

24. Van Terwisga T.J.C., F.P.A., Ziru L., Foeth E.J., *Cavitation erosion - A review of physical mechanisms and erosion risk models*, in *7th International Symposium on Cavitation*. 2009: Ann Arbor, Michigan, USA.

25. Dular, M. and M. Petkovšek, *On the mechanisms of cavitation erosion – Coupling high speed videos to damage patterns.* Experimental Thermal and Fluid Science, 2015. **68**: p. 359-370.

26. Bark G., B.R.E., Grekula M., Berchiche N. *On some physics to consider in numerical simulation of erosive cavitation.* in *7th International Symposium on Cavitation.* 2009. Ann Arbor, Michigan, USA.

27. Osterman, A., B. Bachert, B. Sirok, and M. Dular, *Time dependant measurements of cavitation damage.* Wear, 2009. **266**(9-10): p. 945-51.

28. Bazanini, G. and J.D. Bressan, *Preliminary experience with a new compact disk apparatus for cavitation erosion studies.* Wear, 2007. **263**(1-6): p. 251-7.

29. Bazanini, G., J.D. Bressan, and M.A. Klemz, *Cavitation erosion wear of metallic specimens using the new compact rotating disk device.* Engenharia Térmica (Thermal Engineering), 2008. **7**(1): p. 31-36.

30. Soyama, H. and O. Takakuwa, *Enhancing the Aggressive Strength of a Cavitating Jet and Its Practical Application.* Journal of Fluid Science and Technology, 2011. **6**(4): p. 510-521.

31. Hattori, S., B.-H. Sun, F.G. Hammitt, and T. Okada, *An application of bubble collapse pulse height spectra to venturi cavitation erosion of 1100-o aluminum.* Wear, 1985. **103**(2): p. 119-131.

32. Franc, J.-P. and J.-M. Michel, *Cavitation erosion research in France: the state of the art.* Journal of Marine Science and Technology, 1997. **2**: p. 233-244.

33. Steller, J., A. Krella, J. Koronowicz, and W. Janicki, *Towards quantitative assessment of material resistance to cavitation erosion.* Wear, 2005. **258**(1-4): p. 604-613.

34. Coleman, S.L., V.D. Scott, B. McEnaney, B. Angell, and K.R. Stokes, *Comparison of tunnel and jet methods for cavitation erosion testing.* Wear, 1995. **184**(1): p. 73-81.

35. Franc, J.-P., *Incubation Time and Cavitation Erosion Rate of Work-Hardening Materials.* Journal of Fluids Engineering, 2009. **131**(2): p. 021303.

36. Hattori, S., R. Ishikura, and Q. Zhang, *Construction of database on cavitation erosion and analyses of carbon steel data.* Wear, 2004. **257**(9-10): p. 1022-1029.

37. Hattori, S. and R. Ishikura, *Revision of cavitation erosion database and analysis of stainless steel data.* Wear, 2010. **268**(1-2): p. 109-116.

38. Hattori, S. and N. Mikami, *Cavitation erosion resistance of stellite alloy weld overlays.* Wear, 2009. **267**(11): p. 1954-60.

39. Karimi, A. and J.L. Martin, *Cavitation erosion of materials.* International Metals Reviews, 1986. **31**(1): p. 1-26.

40. Deplancke, T., O. Lame, J.-Y. Cavaille, M. Fivel, M. Riondet, and J.-P. Franc, *Outstanding cavitation erosion resistance of Ultra High Molecular Weight Polyethylene (UHMWPE) coatings.* Wear, 2015. **328–329**(0): p. 301-308.

41. Belahadji, B., J.-P. Franc, and J.-M. Michel, *A Statistical Analysis of Cavitation Erosion Pits.* Journal of Fluids Engineering, 1991. **113**(4): p. 700-706.

42. Franc, J.-P., M. Riondet, A. Karimi, and G.L. Chahine, *Material and velocity effects on cavitation erosion pitting.* Wear, 2012. **274-275**(0): p. 248-259.

43. Franc, J.-P., M. Riondet, A. Karimi, and G.L. Chahine, *Impact Load Measurements in an Erosive Cavitating Flow.* Journal of Fluids Engineering, 2011. **133**(12): p. 121301-8.

44. Soyama, H., Y. Sekine, and K. Saito, *Evaluation of the enhanced cavitation impact energy using a PVDF transducer with an acrylic resin backing.* Measurement, 2011. **44** p. 1279-1283.

45. Wang, Y.-C., C.-H. Huang, Y.-C. Lee, and H.-H. Tsai, *Development of a PVDF sensor array for measurement of the impulsive pressure generated by cavitation bubble collapse.* Experiments in Fluids, 2006. **41**(3): p. 365-373.

46. Momma, T. and A. Lichtarowicz, *A study of pressures and erosion produced by collapsing cavitation.* Wear, 1995. **186-187**(Part 2): p. 425-436.

47. Hattori, S., T. Hirose, and K. Sugiyama, *Prediction method for cavitation erosion based on measurement of bubble collapse impact loads.* Wear, 2010. **269**(7–8): p. 507-514.

48. Zhou, Y.K. and F.G. Hammitt, *Cavitation erosion incubation period.* Wear, 1983. **86**(2): p. 299-313.

49. Hammitt, F.G., *Cavitation Erosion: The State of the Art and Predicting Capability.* Applied Mechanics Reviews, 1979. **32**(6): p. 665-675.

50. Ashby, M.F., *Materials Selection in Mechanical Design*. 2005: Elsevier.

51. Li, D.G., D.R. Chen, and P. Liang, *Enhancement of cavitation erosion resistance of 316 L stainless steel by adding molybdenum.* Ultrasonics Sonochemistry, 2017. **35, Part A**: p. 375-381.

52. Kwok, C.T., H.C. Man, F.T. Cheng, and K.H. Lo, *Developments in laser-based surface engineering processes: with particular reference to protection against cavitation erosion.* Surface and Coatings Technology, 2016. **291**: p. 189-204.

53. Sato, M., O. Takakuwa, M. Nakai, M. Niinomi, F. Takeo, and H. Soyama, *Using Cavitation Peening to Improve the Fatigue Life of Titanium Alloy Ti-6Al-4V Manufactured by Electron Beam Melting.* Materials Sciences and Applications, 2016. **7**: p. 181-191.

54. Münsterer, S. and K. Kohlhof, *Cavitation protection by low temperature TiCN coatings.* Surface and Coatings Technology, 1995. **74-75**(Part 2): p. 642-647.

55. Krella, A. and A. Czyzniewski, *Cavitation erosion resistance of nanocrystalline TiN coating deposited on stainless steel.* Wear, 2008. **265**(7-8): p. 963-970.

56. Krella, A. and A. Czyzniewski, *Influence of the substrate hardness on the cavitation erosion resistance of TiN coating.* Wear, 2007. **263**(1-6): p. 395-401.

57. Hattori, S., K. Taruya, K. Kikuta, and H. Tomaru, *Cavitation erosion of silver plated coatings considering thermodynamic effect.* Wear, 2013. **300**(1–2): p. 136-142.

58. Cheng, F. and S. Jiang, *Cavitation erosion resistance of diamond-like carbon coating on stainless steel.* Applied Surface Science, 2014. **292**: p. 16-26.

59. Zhang, J., W. Richardson M. O, D. Wilcox G, J. Min, and X. Wang, *Assessment of resistance of non-metallic coatings to silt abrasion and cavitation erosion in a rotating disk test rig.* Wear, 1996. **194**(1-2): p. 149-155.

60. Böhm, H., S. Betz, and A. Ball, *The wear resistance of polymers.* Tribology International, 1990. **23**(6): p. 399-406.

61. Frunzaverde, D., C.R. Ciubotariu, E.R. Secosan, C.V. Campian, and C. Fanica, *Study on the Use of Elastomeric Coatings for Protection of Hydraulic Turbine Components Against Cavitation Erosion.* Materiale Plastice, 2016. **53**(3): p. 557-560.

62. Qiu, N., L. Wang, S. Wu, and D.S. Likhachev, *Research on cavitation erosion and wear resistance performance of coatings.* Engineering Failure Analysis, 2015. **55**: p. 208-223.

63. Fairfield, C.A., *Cavitation damage to potential sewer and drain pipe materials.* Wear, 2014. **317**(1–2): p. 92-103.

64. Hattori, S. and T. Itoh, *Cavitation erosion resistance of plastics.* Wear, 2011. **271**(7–8): p. 1103-1108.

65. Arora, H.S., H.S. Grewal, H. Singh, B.K. Dhindaw, and S. Mukherjee, *Unusually high erosion resistance of zirconium-based bulk metallic glass.* Journal of Materials Research, 2013. **28**(22): p. 3185-3189.

66. Drozdz, D., R.K. Wunderlich, and H.J. Fecht, *Cavitation erosion behaviour of Zr-based bulk metallic glasses.* Wear, 2007. **262**(1-2): p. 176-183.

67. Roy, S.C., J.-P. Franc, and M. Fivel, *Cavitation erosion: Using the target material as a pressure sensor*. Journal of Applied Physics, 2015. **118**(16): p. 164905.

68. Roy, S.C., J.-P. Franc, N. Ranc, and M. Fivel, *Determination of cavitation load spectra—Part 2: Dynamic finite element approach.* Wear, 2015. **344–345**: p. 120-129.

69. Sekine, Y. and H. Soyama, *Evaluation of the surface of alloy tool steel treated by cavitation shotless peening using an eddy current method.* Surface and Coatings Technology, 2009. **203**(16): p. 2254-2259.

70. Soyama, H. and F. Takeo, *Comparison between cavitation peening and shot peening for extending the fatigue life of a duralumin plate with a hole.* Journal of Materials Processing Technology, 2016. **227**: p. 80-87.

71. Karimi, A. and W.R. Leo, *Phenomenological Model for Cavitation Rate Computation.* Materials Science & Engineering, 1987. **95**: p. 1-14.

72. Pöhl, F., S. Mottyll, R. Skoda, and S. Huth, *Evaluation of cavitation-induced pressure loads applied to material surfaces by finite-element-assisted pit analysis and numerical investigation of the elasto-plastic deformation of metallic materials.* Wear, 2015. **330–331**: p. 618-628.

73. Roy, S.C., J.-P. Franc, C. Pellone, and M. Fivel, *Determination of cavitation load spectra – Part 1: Static finite element approach.* Wear, 2015. **344–345**: p. 110-119.

74. Fivel, M., J.-P. Franc, and S. Chandra Roy, *Towards numerical prediction of cavitation erosion.* Interface Focus, 2015. **5**(5).

75. Roy, S.C., *Modeling and analysis of material behavior during cavitation erosion*. 2015, Université Grenoble Alpes.